Research Article | Vol. 27, No. 26 / 23 December 2019 / Optics Express 37400
Optics EXPRESS

Visible-light silicon nitride waveguide devices and implantable neurophotonic probes on thinned 200 mm silicon wafers

WESLEY D. SACHER,[1,2,3,*] XIANSHU LUO,[4] YISU YANG,[2] FU-DER CHEN,[2] THOMAS LORDELLO,[2] JASON C. C. MAK,[2,3] XINYU LIU,[1] TING HU,[5] TIANYUAN XUE,[2] PATRICK GUO-QIANG LO,[4] MICHAEL L. ROUKES,[1] AND JOYCE K. S. POON[2,3]

[1]*Division of Physics, Mathematics, and Astronomy, California Institute of Technology, Pasadena, California 91125, USA*
[2]*Department of Electrical and Computer Engineering, University of Toronto, 10 King's College Rd., Toronto, Ontario M5S 3G4, Canada*
[3]*Max Planck Institute of Microstructure Physics, Weinberg 2, 06120, Halle, Germany*
[4]*Advanced Micro Foundry Pte Ltd, 11 Science Park Road, Singapore Science Park II, 117685, Singapore*
[5]*Institute of Microelectronics, A*STAR (Agency for Science, Technology and Research), 11 Science Park Road, Singapore Science Park 11, 117685, Singapore*
[*]*wesley.sacher@mpi-halle.mpg.de*

Abstract: We present passive, visible light silicon nitride waveguides fabricated on ≈ 100 μm thick 200 mm silicon wafers using deep ultraviolet lithography. The best-case propagation losses of single-mode waveguides were ≤ 2.8 dB/cm and ≤ 1.9 dB/cm over continuous wavelength ranges of 466-550 nm and 552-648 nm, respectively. In-plane waveguide crossings and multimode interference power splitters are also demonstrated. Using this platform, we realize a proof-of-concept implantable neurophotonic probe for optogenetic stimulation of rodent brains. The probe has grating coupler emitters defined on a 4 mm long, 92 μm thick shank and operates over a wide wavelength range of 430-645 nm covering the excitation spectra of multiple opsins and fluorophores used for brain stimulation and imaging.

1. Introduction

As foundry-fabricated silicon nitride-on-silicon (SiN-on-Si) photonic platforms on 200 mm and 300 mm substrates for telecommunication wavelengths have rapidly matured in the past several years [1–4], the opportunity opens to consider extending the manufacturing technology of the SiN waveguides to the visible spectrum. SiN is CMOS-compatible and exhibits broadband transparency that, in principle, extends into the visible spectrum. Visible light integrated photonics can address new applications in atomic physics and quantum information, fluorescence excitation and sensing, optogenetics, and imaging and display. However, challenges in fabrication and characterization arise in realizing integrated photonics devices in the visible spectrum when compared to telecommunication wavelengths near 1310 nm or 1550 nm. First, the waveguide and device dimensions are smaller, especially in the blue-end of the spectrum, to maintain the single-mode or few-mode condition. Second, the mode confinement in the waveguide is also higher at short wavelengths, which leads to higher sensitivity to surface roughness scattering and tighter fabrication tolerances. Therefore, low-loss waveguides require excellent control over the dimensions, sidewall and surface roughness, and material absorption. Beyond the fabrication, the lack of swept-wavelength laser sources across the entire visible spectrum may also limit the comprehensive characterization of fabricated devices.

#375224 https://doi.org/10.1364/OE.27.037400
Journal © 2019 Received 26 Aug 2019; revised 6 Nov 2019; accepted 11 Nov 2019; published 11 Dec 2019

Optics EXPRESS

To date, single-mode visible light waveguides have been demonstrated using SiN [5–7] and alumina (Al_2O_3) [8,9] on 200 mm or 300 mm Si wafers, and using aluminum nitride (AlN) with chip-scale fabrication [10]. However, in all of these demonstrations, waveguide losses were only reported at discrete wavelengths, and complete, continuous waveguide loss spectra were not obtained. In [5] on 200 mm wafers, single-mode SiN waveguides formed by plasma enhanced chemical vapour deposition (PECVD) exhibited a loss of about 1 dB/cm at a wavelength of 532 nm. In [8,9], SiN waveguide losses $\leq$ 20.7 dB/cm and Al_2O_3 waveguide losses $\leq$ 1.6 dB/cm were observed at 4 discrete wavelengths between 405 nm and 458 nm; losses as low as 4.8 and 0.6 dB/cm were observed at 458 nm for the SiN and Al_2O_3 waveguides, respectively. Although SiN generally exhibited higher losses than Al_2O_3 in that demonstration, the CMOS compatibility and fabrication maturity of SiN makes it a promising material for further development for visible light integrated photonics platforms.

In this article, we present low-temperature PECVD and high-temperature low pressure chemical vapour deposition (LPCVD) SiN waveguides with SiO_2 cladding formed on 200 mm Si wafers using the Advanced Micro Foundry (AMF) foundry process and their application in implantable neuroprobes. The loss spectra of the waveguides were fully characterized in the visible spectrum using a supercontinuum light source for both orthogonal polarizations. Propagation losses $\leq$ 2.8 dB/cm and $\leq$ 1.9 dB/cm were observed for the best performing single-mode PECVD SiN waveguides over 466-550 nm and 552-648 nm wavelength ranges, respectively. We also demonstrate waveguide crossings and power splitters based on multimode interference (MMI) couplers. The waveguide losses are sufficiently low to be suitable for further demonstrations and developments of visible light photonic integrated circuits on Si substrates. Finally, as an example application, we demonstrate implantable neuroprobes for optogenetic stimulation using the PECVD SiN waveguides.

2. Waveguide geometry and fabrication

The cross-section of the SiN waveguides is shown in Fig. 1(a). A thin SiN waveguide layer with SiO_2 cladding is defined above a bulk Si substrate. The SiN, bottom cladding, and top cladding thicknesses are t_{SiN}, $t_{clad,\,bot}$, and $t_{clad,\,top}$, respectively. t_{SiN} is chosen to be thick enough for moderate to high optical confinement across the visible spectrum while thin enough for single-mode operation at blue wavelengths with waveguide widths > 200 nm, which are attainable with deep ultraviolet (DUV) lithography. $t_{clad,\,bot}$ and $t_{clad,\,top}$ are thick enough for negligible absorption by the Si substrate or absorbing material in contact with the superstrate.

Three variations of SiN waveguides are explored in this work, and one wafer was characterized for each, which are referred to as Wafer 1, Wafer 2, and Wafer 3. The SiN type and the thicknesses of the waveguide layer, top cladding, and bottom cladding are summarized in Table 1.

Table 1. Variations of SiN waveguides fabricated

	SiN Type	t_{SiN}	$t_{clad,top}$	$t_{clad,bot}$
Wafer 1	PECVD	200 nm	1.2 μm	1.48 μm
Wafer 2	PECVD	135 nm	1.55 μm	1.48 μm
Wafer 3	LPCVD	200 nm	1.2 μm	1.48 μm

The waveguides and devices were fabricated on 200 mm diameter Si wafers. The SiO_2 bottom cladding and SiN waveguide layer were deposited first. Fully-etched SiN waveguides were formed by DUV lithography and reactive-ion etching (RIE). The SiO_2 top cladding was deposited and deep trenches were etched to form edge couplers. Chemical mechanical planarization (CMP) was used to planarize layers. Finally, backgrinding was used to thin the wafers to $\approx$ 100 μm similar to the procedure in [11]. Additional wafers were fabricated with $\approx$ 50 μm thicknesses, however, at the time of writing, they have not been fully characterized. The whole-wafer thinning

Optics EXPRESS

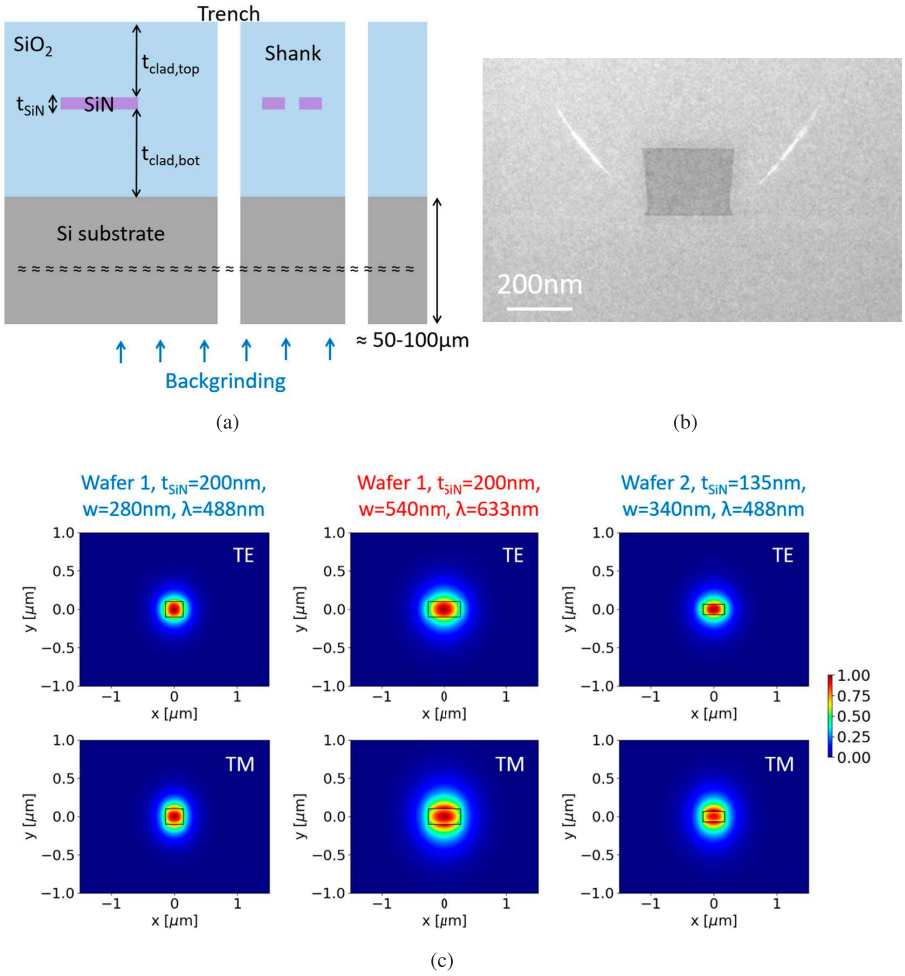

Fig. 1. (a) Schematic of the SiN waveguide platform. t_{SiN}, $t_{clad,\,bot}$, and $t_{clad,\,top}$ are the SiN, bottom SiO_2 cladding, and top SiO_2 cladding thicknesses, respectively. Wafer backgrinding is used to thin the wafers for the neurophotonic probe application. (b) Cross-section transmission electron micrograph (X-TEM) of a single-mode waveguide from Wafer 1. (c) Simulated mode profiles at wavelengths (λ) 488 nm and 633 nm of waveguides from Wafers 1 and 2. The electric field magnitudes $|E_x|$ and $|E_y|$ are shown for the TE and TM polarizations, respectively.

is optional but was carried out for the purpose of testing the fabrication process of implantable neuroprobes for optogenetic stimulation and functional optical imaging [12,13]. This etching before grinding technique (auto-dicing) also separated the dies on the grinding tape since test dies were surrounded on all sides by deep trenches. A cross-section transmission electron micrograph (X-TEM) of a fabricated 270 nm wide SiN waveguide from Wafer 1 is shown in Fig. 1(b). X-TEMs and cross-section scanning electron micrographs of a small number of dies from Wafers 1-3 confirmed the SiN thicknesses.

The measured PECVD and LPCVD SiN refractive indices monotonically decreased from 1.82-1.79 and 2.02-1.98, respectively, over a wavelength range of 450-648 nm. Mode profiles and single-mode cutoff widths were calculated using a finite difference eigenmode solver with the nominal SiN thicknesses and measured refractive indices. The widths for the single-mode

Optics EXPRESS

condition are summarized in Table 2. We defined the cutoff condition as the largest waveguide width (to the nearest 10 nm increment) where the calculated effective indices of all higher order modes were $< 10^{-4}$ above the cladding index.

Table 2. SiN refractive indices and single-mode cutoff waveguide widths

	Refractive index λ = 450 − 648 nm	λ = 450 nm	λ = 488 nm	λ = 532 nm	λ = 633 nm
Wafer 1	1.82 - 1.79	340 nm	390 nm	440 nm	580 nm
Wafer 2	1.82 - 1.79	410 nm	470 nm	540 nm	> 700 nm
Wafer 3	2.02 - 1.98	240 nm	270 nm	320 nm	410 nm

3. Measurement results

To measure waveguide loss and device loss spectra across the visible spectrum, the measurement setup in Fig. 2(a) was used. A 20 W supercontinuum laser (Fianium WhiteLase SC480-20) was coupled to a narrowband tunable optical filter (Photon Etc. LLTF Contrast VIS HP20). The full-width-at-half-maximum (FWHM) linewidth of the filter was < 2 nm over a wavelength range from 430 to 648 nm. The free-space output of the filter was passed through a polarizer and coupled to a polarization-maintaining (PM) fiber (Nufern PM460-HP). The axis of the polarizer was aligned to the slow-axis of the PM fiber, and the opposite end of the PM fiber was cleaved for edge-coupling to the photonic chip. This end of the fiber was mounted in a 5-axis micromanipulator with a fiber rotation mount for aligning the fiber to on-chip edge couplers [Fig. 2(b)] and aligning the slow-axis of the fiber with the principal axes of the chip for either transverse-electric (TE) or transverse-magnetic (TM) light injection. Prior to chip measurements, a free-space polarizer was placed in front of the fiber facet to verify the polarization extinction ratio was > 20 dB over a wavelength range of 430-648 nm and to identify the angle of the fiber slow axis within the rotation mount. A cleaved single-mode (SM) fiber (Nufern 460-HP) was coupled to edge couplers on the output facet of the chip, Fig. 2(c), and the fiber was connected to an optical detector for detection of output light from the chip.

Transmission spectra of on-chip waveguides and devices were collected under computer control by stepping the center wavelength of the tunable optical filter in 2 nm steps and measuring the fiber-coupled output power of the chip for each wavelength. Simultaneously, a second detector measured the tapped input power to the chip to verify the input optical power did not drift, as shown in Fig. 2(a). The wavelength range of measurements was fixed to 430-648 nm. The lower end was limited by the single-mode cut-off wavelengths of the fibers (specified as 410 ± 40 nm and 430 ± 20 nm for PM460-HP and 460-HP, respectively). Single-mode operation of the fibers between 430-450 nm is not guaranteed, however, reasonable fits and reproducibility in cutback measurements indicates multimode behaviour was not significant.

Tapered edge couplers were used for fiber-to-chip coupling on all devices in the platform. The waveguide width was 5.2 μm at the chip facet and narrowed over a 400 μm length to a single-mode waveguide width. Coupling efficiencies for the edge couplers were measured for Wafers 1-3 by measuring the transmission spectrum of a straight waveguide with edge couplers at each facet and normalizing to the measured power at the input fiber facet. The loss of the 1.798 mm long straight waveguide between the edge couplers was not de-embedded from the edge coupler loss. The measured coupling efficiencies are shown in Fig. 3. For the TE polarization, the edge coupler coupling efficiency was −7.9 to −9.8 dB/facet, −8.0 to −8.9 dB/facet, and −8.5 to −11.3 dB/facet for Wafers 1, 2, and 3, respectively, over a 430-648 nm wavelength range. For the TM polarization, the edge coupler coupling efficiency was −7.5 to −8.9 dB/facet, −6.9 to −7.9 dB/facet, and −8.1 to −10.2 dB/facet for Wafers 1, 2, and 3, respectively, over a 430-648 nm

Optics EXPRESS

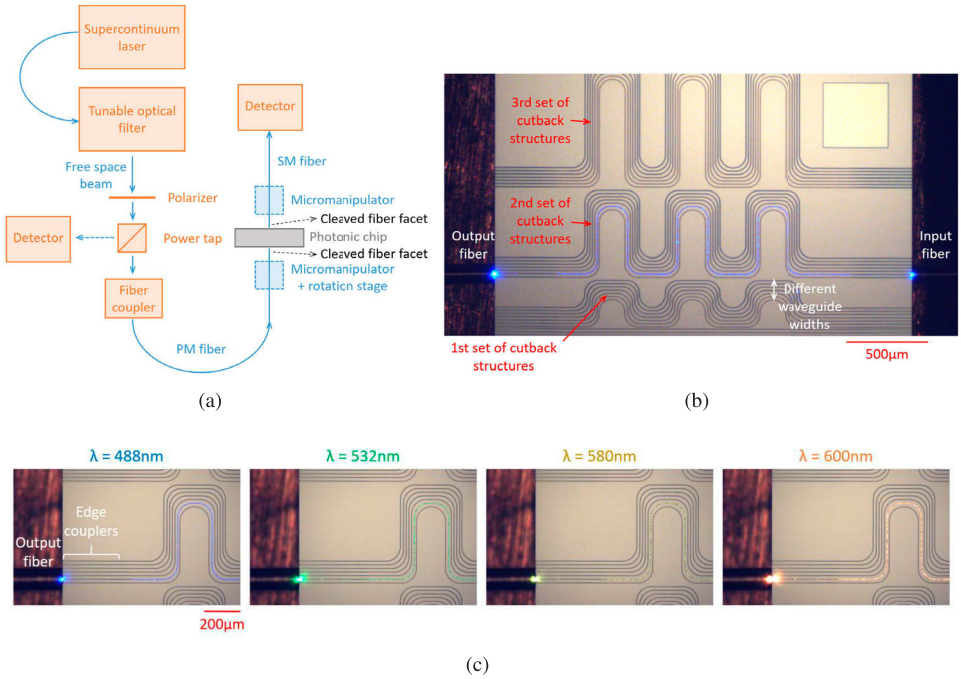

Fig. 2. (a) Schematic of measurement setup. Filtered and polarized light from a supercontinuum laser is coupled into a polarization-maintaining (PM) fiber and edge-coupled to the photonic chip. Output light is collected by a single-mode (SM) fiber edge-coupled to the opposite facet of the chip and detected. (b) Optical micrograph of one of the test chips with waveguide loss cutback structures showing the input and output fibers edge-coupled to the chip. (c) Output facet of the chip in (b) with different wavelength settings of the optical filter.

wavelength range. The TM coupling efficiency was higher than the TE efficiency for all wafers due to the lower optical confinement of the fundamental TM mode and better mode match to the ≈ 3.5 μm mode field diameter of the fiber. The higher efficiency of the Wafers 1 and 2 edge couplers was due to the lower refractive index and resulting reduced optical confinement of the PECVD SiN compared to the LPCVD SiN of Wafer 3. The use of two different fiber types for the input and output coupling in the edge coupler measurements is justified by the similar mode field diameters of the fibers. To confirm the accuracy of the measurements, additional measurements were performed with only 460-HP fiber used for both input and output coupling and optical input from a 473 nm diode laser. The edge coupler efficiencies from these measurements and those in Fig. 3 agree to within 0.2, 0.1, and 0.7 dB/facet for Wafers 1-3, respectively. The error in these measurements are limited by fiber alignment to < 0.2 dB.

3.1. Waveguide loss

Waveguides losses were measured using the cutback method. Microscope images of a subset of the cutback structures are shown in Figs. 2(b) and 2(c). 5 cutback structures were used for each waveguide loss measurement with lengths 0, 1.5, 3, 5.4, and 6.24 mm or 0, 1.5, 3, 6, and 7.2 mm, relative to the shortest structure. The cutback structures used large 80 μm radius bends. Waveguides of different widths, both single-mode and multimode over the majority of the visible spectrum, were measured on 4 dies from both Wafers 1 and 3 and 3 dies from Wafer 2. Both TE and TM polarization losses were measured by rotating the input PM fiber to select the input polarization. The cutback structures for the multimode waveguides had a short length of

Optics EXPRESS

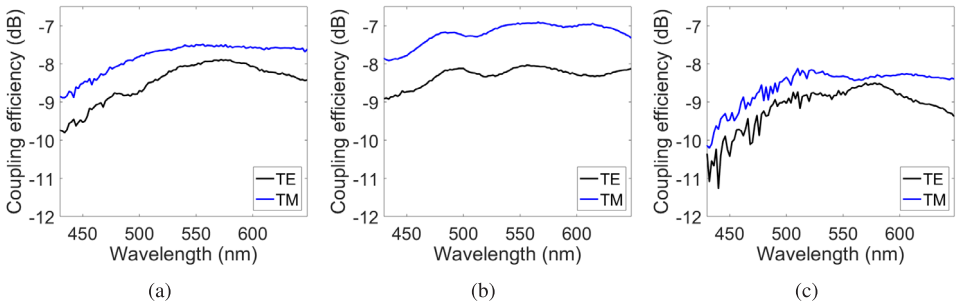

Fig. 3. Measured coupling efficiency per facet for edge couplers from (a) Wafer 1, (b) Wafer 2, (c) Wafer 3 for TE and TM polarizations.

single-mode waveguide following the input edge coupler to strip off higher order modes injected by the input fiber.

Figure 4(a) shows an example of the measured optical power spectrum from a set of cutback structures on Wafer 1. Since this plot is the raw fiber-coupled output power from the chip, much of the spectral dependence of the power is due to the spectral power distribution of the supercontinuum laser. Figure 4(d) shows linear fitting of the losses of the cutback structures versus relative waveguide length at multiple wavelengths; the goodness of fit is high with $R^2 > 0.97$.

Waveguide loss spectra extracted via the cutback method are shown in Figs. 4–6 for the TE and TM polarizations. Waveguide widths were measured using X-TEM and X-SEM imaging. Single-mode waveguides at red, green, and blue wavelengths as well as multimode waveguide were measured. For Wafer 1, the simulated single-mode cutoff wavelengths are < 430 nm and 610 nm for the 280 nm and 540 nm wide waveguides, respectively. For Wafer 2, the single-mode cutoff wavelengths are < 430 nm, < 430 nm, and 525 nm for the 270 nm, 340 nm, and 520 nm wide waveguides, respectively. Finally, for Wafer 3, the single-mode cutoff wavelengths are 470 nm, 515 nm, and > 650 nm for the 250 nm, 290 nm, and 520 nm wide waveguides, respectively. Ripple occurs throughout the 520-540 nm wide waveguide loss spectra and at short wavelengths close to and below the single-mode cutoff wavelength for the narrower waveguides. As explained in the Appendix, this is most likely due to excitation and interference of higher order modes. This ripple and fiber alignment error are the primary sources of error in the cutback measurements and are quantified in the standard errors listed below. To reduce alignment error, the fiber alignment process was automated. For Wafer 2, spectra were terminated at wavelengths above which the optical confinement became sufficiently low for bend losses and substrate absorption to prevent an accurate linear fit of the cutback structure losses.

The waveguide loss measurements are summarized in Table 3. For all wafers, the losses decreased with increasing waveguide width due to reduced modal overlap with the etched sidewalls. Wafer 2 showed the lowest losses at blue and green wavelengths between 430-550 nm likely due to the thinner SiN compared to Wafers 1 and 3, which results in a lower modal overlap with the etched sidewalls. For Wafer 2, the average waveguide losses for the single-mode 340 nm wide waveguide from 466-500 nm were ≤ 4.1 dB/cm and ≤ 2.8 dB/cm for the TE and TM polarizations, respectively. From 502-550 nm, the average waveguide losses were ≤ 3.3 dB/cm and ≤ 2.3 dB/cm for the TE and TM polarizations, respectively. The blue-green (466-550 nm) single-mode waveguide losses (280 nm width) on Wafer 1 were ≤ 8.8 dB/cm. Wafer 3 generally exhibited the highest losses at blue and green wavelengths. This may be due to the higher refractive index of the LPCVD SiN causing increased sidewall scattering. This may also be due to the absorption mechanism noted in [9] at wavelengths close to and below 400 nm. However, since the exact roughness of each wafer was not quantified, variations in roughness

Optics EXPRESS

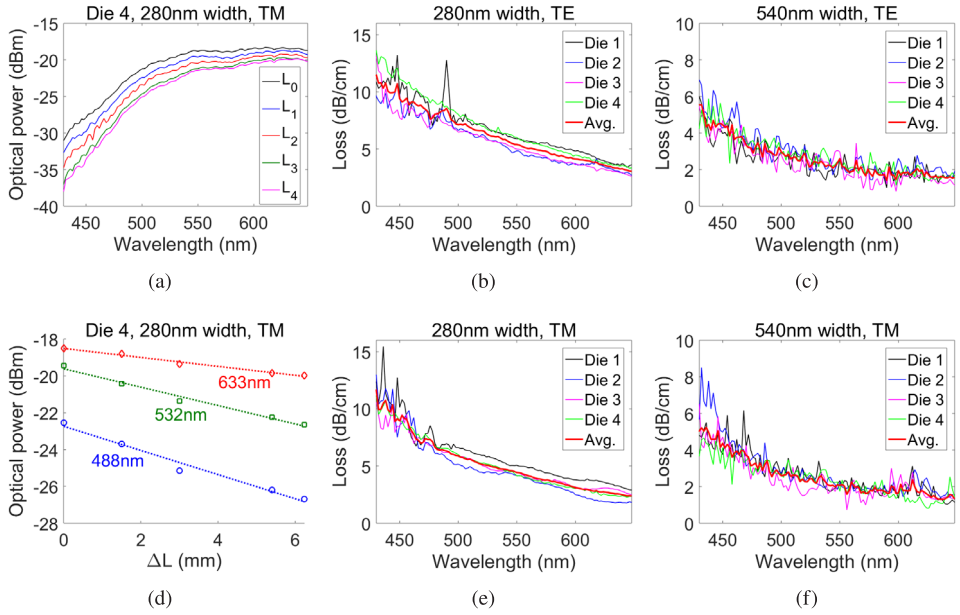

Fig. 4. Wafer 1 waveguide loss cutback measurements. (a), (d) Example measurement showing (a) output power spectra of the cutback structures (L_0-L_4) for 280 nm wide waveguides from Die 4 (TM polarization) and (d) the corresponding linear fits of the output power versus length showing extraction of the waveguide losses at 488 nm, 532 nm, and 633 nm wavelengths. (b), (e) Waveguide losses of 280 nm wide waveguides for (b) TE- and (e) TM-polarized light. (c), (f) Losses of 540 nm wide waveguides for (c) TE- and (f) TM-polarized light. The red waveguide loss traces are averages (Avg.) of Dies 1-4. The median (90th percentile) of the standard errors of the Avg. traces over the measurement wavelength range are (b), (e) 0.7-0.8 (1.3-1.4) dB/cm and (c), (f) 0.4-0.5 (0.7-0.9) dB/cm.

between the wafers may also contribute to this observation. At yellow and red wavelengths > 552 nm, the differences in waveguide loss between the wafers was marginal. The best performing single-mode waveguides from 552-648 nm were the 520 nm wide Wafer 2 waveguides with TE polarization losses ≤ 1.9 dB/cm; closely followed by the Wafer 3 - 290 nm wide and Wafer 1 - 280 nm wide waveguides with TM polarization losses ≤ 3.4 dB/cm and ≤ 4.4 dB/cm, respectively.

The thin PECVD SiN on Wafer 2 appears to provide a significant waveguide loss advantage over Wafers 1 and 3 at blue and green wavelengths. However, this comes at the expense of reduced optical confinement. Designs requiring maximum optical confinement may benefit from the parameters of Wafers 1 or 3 and mitigate waveguide loss by using only short lengths of single-mode waveguides and long lengths of multimode waveguides.

The waveguide loss standard errors averaged over the measurement wavelength range for each individual waveguide loss spectrum in Figs. 4–6 ranged from 0.3 - 1.3 dB/cm, 0.3 - 0.9 dB/cm, and 0.3 - 1.5 dB/cm for Wafers 1-3, respectively. The average values are stated because the cutback structure transmission spectra ripple discussed in the Appendix leads to wavelength-dependent standard errors. The ripple is not correlated across dies and the average waveguide loss traces have less wavelength-dependent standard errors, which is evident in the median and 90th percentile (over wavelength) standard errors listed in the captions of Figs. 4–6.

Bend losses were also measured with cutback structures with increasing numbers of 90° waveguide bends. The extracted loss per 90° bend included the bend mode radiation losses, the mode overlap losses between the bend mode and input/output straight waveguide modes, and

Optics EXPRESS

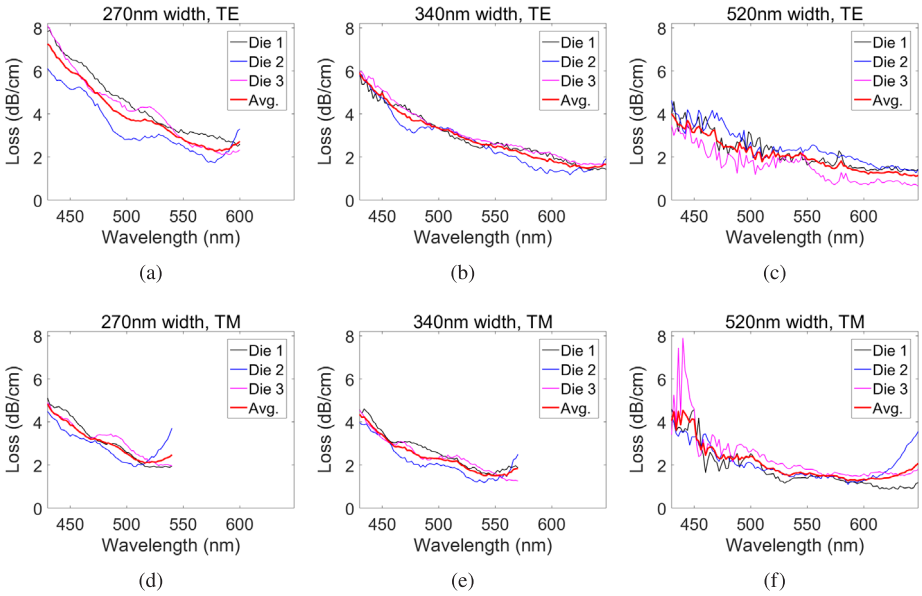

Fig. 5. Wafer 2 waveguide loss cutback measurements for (a),(d) 270 nm, (b),(e) 340 nm, and (c),(f) 520 nm wide waveguides. The top row (a)-(c) is for the TE polarization, and the bottom row (d)-(f) is for the TM polarization. The median (90th percentile) of the standard errors of the Avg. traces over the measurement wavelength range are 0.5 (0.6-0.8) dB/cm.

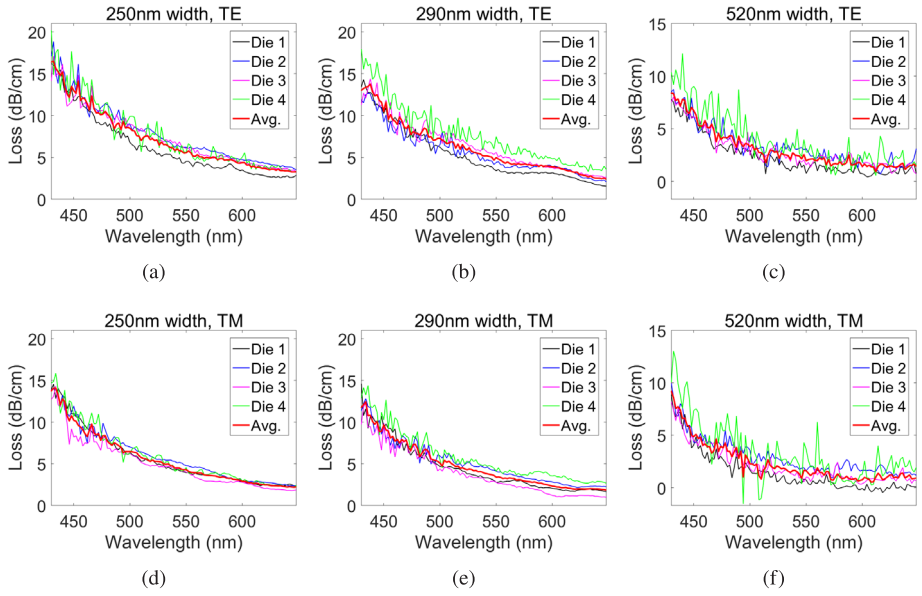

Fig. 6. Wafer 3 waveguide loss cutback measurements for (a),(d) 250 nm, (b),(e) 290 nm, and (c),(f) 520 nm wide waveguides. The top row (a)-(c) is for the TE polarization, and the bottom row (d)-(f) is for the TM polarization. The median (90th percentile) of the standard errors of the Avg. traces are (a),(b),(d),(e) 0.5-0.7 (1.3) dB/cm, (c),(f) 0.6-0.7 (0.9) dB/cm.

Optics EXPRESS

Table 3. Summary of average waveguide (Wg.) losses for TE and TM polarizations (Pol.) over various wavelength (λ) ranges

Wafer	Wg. width (nm)	Pol.	Loss λ = 430-464nm (dB/cm)	Loss λ = 466-500nm (dB/cm)	Loss λ = 502-550nm (dB/cm)	Loss λ = 552-600nm (dB/cm)	Loss λ = 602-648nm (dB/cm)
1 PECVD t_{SiN} = 200nm	280	TE	8.9-11.5	7.1-8.8	5.4-7.2	4.1-5.4	3.1-4.1
		TM	7.4-11.7	5.9-7.4	4.4-5.8	3.1-4.4	2.4-3.1
	540	TE	3.6-5.5	2.7-3.8	2.1-2.9	1.4-2.5	1.5-2.1
		TM	3.6-5.2	2.5-4.0	2.0-2.8	1.6-2.3	1.3-2.4
2 PECVD t_{SiN} = 135nm	270	TE	5.5-7.3	3.8-5.3	2.8-3.8	2.3-2.7	N/A
		TM	3.3-4.8	2.5-3.3	2.1-2.5[a]	N/A	N/A
	340	TE	4.1-5.9	3.3-4.1	2.4-3.3	1.8-2.5	1.5-1.8
		TM	2.8-4.4	2.3-2.8	1.5-2.3	1.5-1.8[b]	N/A
	520	TE	3.0-4.0	2.2-3.3	1.8-2.3	1.3-1.9	1.1-1.3
		TM	2.5-4.5	2.2-2.8	1.5-2.4	1.3-1.6	1.3-2.1
3 LPCVD t_{SiN} = 200nm	250	TE	10.6-16.5	8.3-12.4	5.5-8.2	4.3-5.8	3.3-4.4
		TM	8.3-14.1	6.3-9.8	4.3-6.4	2.9-4.1	2.2-2.9
	290	TE	8.9-13.8	7.0-9.4	4.7-7.1	3.9-4.8	2.4-3.8
		TM	7.5-12.4	5.1-7.9	3.4-5.4	2.3-3.4	1.8-2.3
	520	TE	5.1-8.4	3.2-5.4	1.8-3.5	1.4-2.5	0.9-1.7
		TM	3.9-9.2	1.0-4.6	0.8-2.7	0.6-1.9	0.5-1.4

[a] Wavelength span truncated to 502-540 nm
[b] Wavelength span truncated to 552-570 nm

Optics EXPRESS

waveguide propagation losses. For Wafer 1, 20 μm radius bends had $\leq$ 0.05 dB/bend for 280 nm wide waveguides over the wavelength range 430-592 nm for TE and TM polarizations. Above this wavelength range, the bend losses increased significantly due to reduced optical confinement. At longer wavelengths, wider waveguides closer to the single-mode cutoff are more appropriate for small bends, e.g., 20 μm radius bend losses with 340 nm wide waveguides were $\leq$ 0.05 dB/bend for wavelengths between 450-648 nm and 450-620 nm for the TE and TM polarizations, respectively. For Wafer 2, 20 μm radius bend losses for 340 nm wide waveguides were $\leq$ 0.06 dB/bend from 430-522 nm for the TE polarization and $<$ 0.3 dB/bend from 430-490 nm for the TM polarization. At the same waveguide width, 80 μm radius bend losses were $\leq$ 0.06 dB/bend from 430-648 nm and 430-600 nm for the TE and TM polarizations, respectively. For Wafer 3, 20 μm radius bend losses were $\leq$ 0.05 dB/bend for a 290 nm waveguide width from 450-648 nm for TE and TM polarizations. The standard errors on the measurements were $<$ 0.02 dB/bend for Wafers 1 and 2 and $<$ 0.03 dB/bend for Wafer 3 over the measurement wavelength range.

3.2. Waveguide crossing

We used the waveguides to realize several devices that are useful for photonic circuits in the visible spectrum. The first is a waveguide crossing using multimode interference (MMI). In-plane MMI waveguide crossings [14] were designed using finite difference time domain (FDTD) simulations. Crossings were fabricated and measured on each wafer, and an optical microscope image of one of the crossings is shown in Fig. 7(c). An example simulated top-down electric field profile is shown in Fig. 7(b) showing the operation of the device; interference between TE0/TM0 and TE2/TM2 modes excited in the multimode section reduces optical overlap with the discontinuity created by the intersecting waveguides. The same design was used for all wafers with the input and output waveguide widths w_{IO} = 300 nm, taper length L_{taper} = 3 μm, multimode section length L_{MM} = 6.4 μm, and multimode section width w_{MM} = 1 μm. The crossing design dimensions are defined in Fig. 7(a).

Crossing losses were measured using cutback structures with 1, 15, 30, and 45 crossings. Figure 7(d) shows example linear fits of the cutback structure output power versus the number of crossings at multiple wavelengths. $R^2 > 0.9$ for all crossing cutback measurements over the full measurement wavelength range. The standard error of all linear fits was $\leq$ 0.02 dB/crossing for all measurements. Crossing loss spectra are shown in Fig. 8. The minimum loss per crossing ranged from 0.07-0.09 dB/crossing, the loss was $<$ 0.1 dB/crossing for at least a 58 nm bandwidth in all cases, and the loss was $<$ 0.2 dB/crossing for at least a 138 nm bandwidth in all cases.

The optical crosstalk of waveguide crossings was measured by sending light into Input 1 in Fig. 7(c), measuring the power at the crosstalk port (Output 2), and normalizing to the measured power at the thru port (Output 1). The analagous procedure was performed for Input 2 generating two crosstalk measurements for each polarization as shown in Fig. 9. The crosstalk was < -20 dB in all cases over the full measurement bandwidth. Over the 0.1 dB-bandwidth of the crossings, the maximum measured crosstalk was −26(49) dB, −21(47) dB, and −27(32) dB for Wafers 1-3, respectively, for the TE(TM) polarization.

3.3. MMI 1×2 power divider

A second related device is a 1×2 MMI power divider [15]. The devices were designed using FDTD simulations, fabricated, and measured on all three wafers. An optical micrograph of one of the MMI power dividers is shown in Fig. 10(a). Figure 10(b) shows an example top-down electric field intensity profile of light propagating through the MMI divider. The design parameters are: aperture width w_{ap}, output aperture spacing d_{ap}, multimode section length L_{MMI}, and multimode section width w_{MMI}. Three designs were tested. Design 1 (w_{ap} = 360 nm, d_{ap} = 760 nm, L_{MMI} = 4.74 μm, w_{MMI} = 1.52 μm) is a blue wavelength design for Wafers 1 and 3, Design 2 (w_{ap} = 360 nm, d_{ap} = 760 nm, L_{MMI} = 4.14 μm, w_{MMI} = 1.52 μm) is a yellow wavelength

Optics EXPRESS

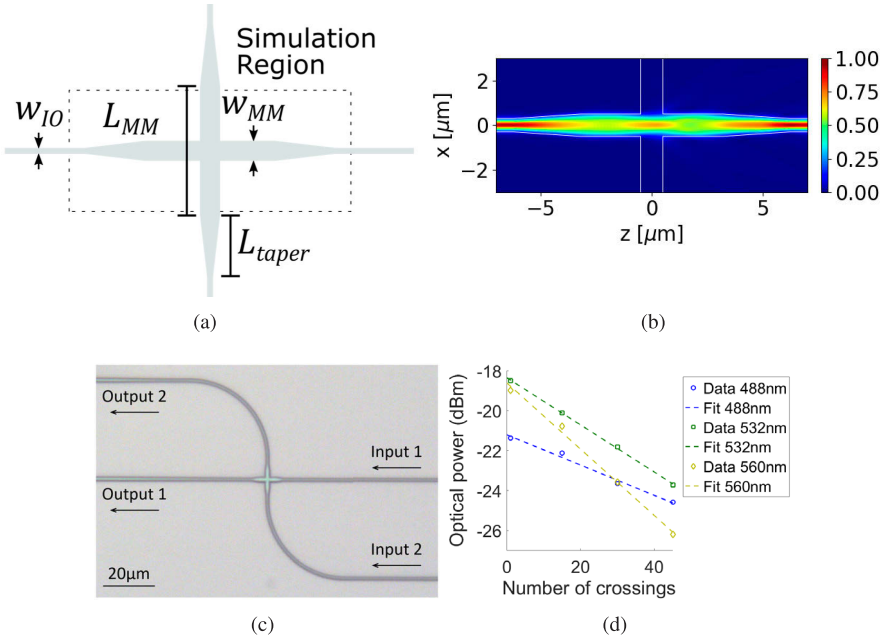

Fig. 7. (a) Schematic of the MMI crossing design defining the design parameters. (b) Wafer 1 crossing top-down electric field profile ($|E_x|$) through the center of the SiN layer simulated by the FDTD method (484.8 nm wavelength, TE polarization). The input is at the far left. (c) Optical micrograph of a waveguide crossing from Wafer 1. (d) Example waveguide crossing loss cutback measurements and linear fits at different wavelengths (Wafer 1, TE).

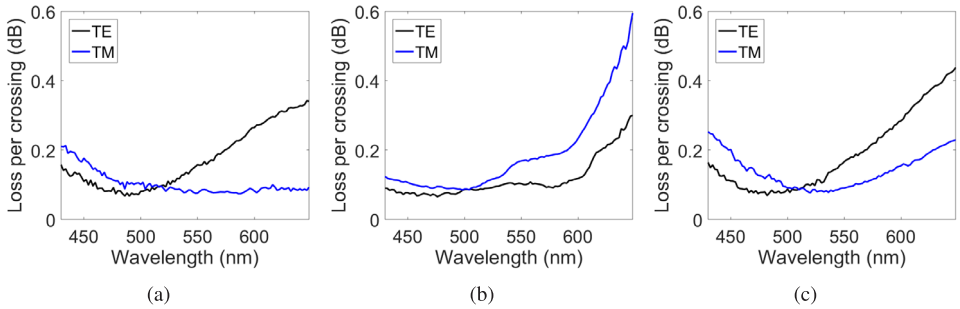

Fig. 8. Measured loss per crossing spectra for waveguide crossings from (a) Wafer 1, (b) Wafer 2, and (c) Wafer 3 for TE and TM polarizations.

Optics EXPRESS

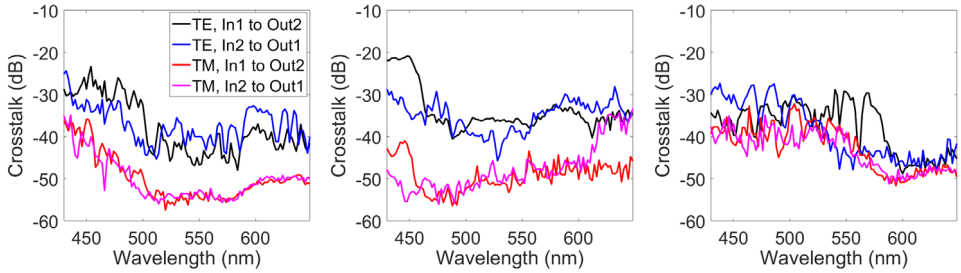

Fig. 9. Measured crossing crosstalk from (a) Wafer 1, (b) Wafer 2, and (c) Wafer 3 for TE and TM polarizations. The legend in (a) also applies to (b) and (c). Crosstalk from both inputs is shown, i.e., input at In1 (Input 1) and crosstalk measured at Out2 (Output 2), and input at In2 (Input 2) and crosstalk measured at Out1 (Output 1); using the input and output naming conventions in Fig. 7(c).

design for Wafer 1, and Design 3 (w_{ap} = 380 nm, d_{ap} = 860 nm, L_{MMI} = 5.44 μm, w_{MMI} = 1.64 μm) is a blue wavelength design for Wafer 2.

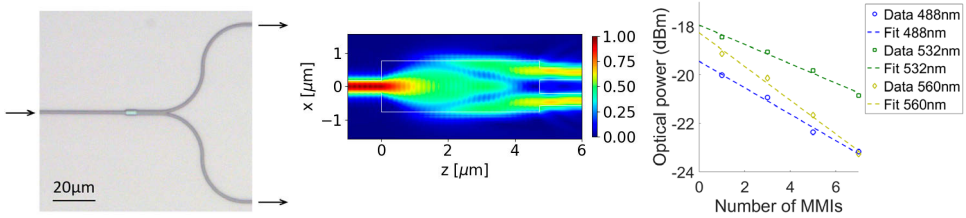

Fig. 10. (a) Optical micrograph of an MMI 1 × 2 power divider from Wafer 1. (b) Design 1 - Wafer 1 top-down electric field intensity profile ($|E_x|^2$) through the center of the SiN layer (FDTD simulation, 484.8 nm wavelength, TE polarization). (c) Example 1 × 2 MMI divider loss cutback measurements and linear fits at different wavelengths (Wafer 1, Design 1, TM). 3-dB losses from each MMI divider due to power division have been subtracted from each data point such that the slope of the linear fit represents excess loss per MMI power divider.

Cutback measurements were performed to characterize the excess loss of the MMI power dividers, i.e., the loss of each output beyond 3 dB due to power division. Cutback structures with 0, 1, 3, and 7 or 1, 3, 5, and 7 MMI dividers were used. Figure 11 shows the excess loss spectra of the MMI power dividers. The various MMI dividers exhibited minimum excess insertion losses between 0.19-0.47 dB and bandwidths over which the excess loss is < 1 dB between 70-172 nm. Similar to Section 3.1, for Wafer 2, excess loss spectra were terminated at wavelengths above which the the optical confinement became low enough for bend losses and substrate absorption to compromise the accuracy of the linear fits of the cutback structure losses. The standard error of the measured MMI divider loss averaged over the 1-dB bandwidth was < 0.06 dB for Wafers 1 and 3 and < 0.08 dB for Wafer 2.

Additional measurements were performed for splitting ratio characterization. Structures with one MMI power divider with both outputs directly connected to edge couplers were measured. Within the 1-dB excess loss bandwidth of the MMI dividers, the splitting ratios were within 1.1 dB of 50:50, with the measurements limited by variations in the edge coupler efficiencies, losses of the routing waveguides, and spectral ripple of the two output paths. More precise measurements of the splitting ratios could be obtained using on-chip Mach-Zehnder interferometers.

Optics EXPRESS

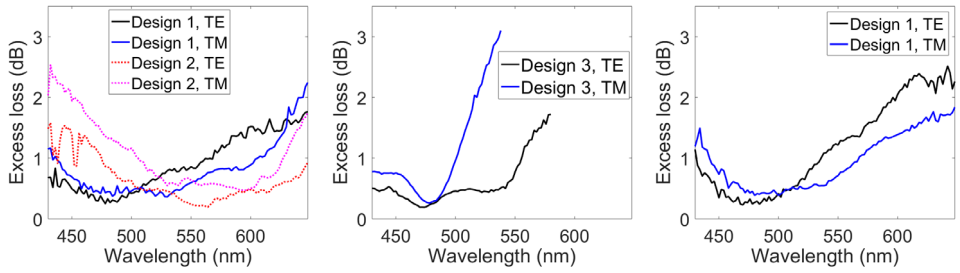

Fig. 11. Measured excess loss per MMI power divider spectra for (a) Wafer 1, (b) Wafer 2, and (c) Wafer 3 for TE and TM polarizations.

4. Application: Implantable neurophotonic probes

Recently, SiN waveguides integrated onto implantable silicon probes ("neurophotonic probes") have been demonstrated for optical stimulation of rodent brains [16–19]. Via optogenetics, neurons can be genetically modified to express light-gated ion channels or pumps (e.g., channelrhodopsin-2), enabling optical stimulation or silencing of neuronal activity [20]. SiN waveguide grating couplers enable low divergence beams [17,18], light sheets [13], and steerable beams via phased arrays [12] to be emitted into brain tissue for high-resolution patterned optical stimulation of brain tissue. The waveguides can be integrated onto long, thin, needles ("shanks") that can penetrate deep into the brain with minimal tissue damage.

Wafers 1-3 were thinned to 92-100 μm enabling the demonstration of neurophotonic probes with integrated SiN waveguides. Additional wafers were fabricated and thinned to $\approx$ 50 μm, however at the time of writing, the characterization of these wafers was not complete. Here, we focus on the characterization of a probe chip from Wafer 2 with a thickness of 92 μm. The neurophotonic probe, Fig. 12(a), has an array of edge couplers for coupling light from a multi-core fiber or image bundle for addressing multiple waveguides via external scanning optics or spatial light modulators, as demonstrated in [12,13,21]. The edge coupler design is the same as that characterized in Section 3, and 100 μm lengths of single-mode waveguides follow the edge couplers. Subsequently, the waveguides are widened to multimode waveguide widths between 0.6-1 μm, routed down the shank, and terminated with grating couplers with a 440 nm pitch and 6 μm socket width to generate the output beams radiated from the shank. The staggered array of 21 grating couplers are on 54 μm longitudinal and lateral pitches. The shank width linearly tapers from 90 μm to 72 μm down the 4 mm shank length, and subsequently tapers to a tip, Fig. 12(b).

The neurophotonic probe was characterized using a single-mode optical fiber (Nufern 460-HP) aligned to the various edge couplers as in Fig. 13(a). The fiber delivered light from a supercontinuum laser via a wavelength tunable filter and an inline fiber polarization controller. A droplet of optically opaque epoxy was placed and cured on top of the base of the chip above the edge couplers and waveguide fan-in to block stray input light not coupled into the edge couplers; no epoxy was on the shank. Transmission through all grating coupler outputs was verified, Fig. 12(c), and the transmission spectrum and far field radiation patterns were measured for the most distal grating coupler, Fig. 12(d). First and second order diffracted output beams were observed with wavelength and polarization dependent powers as shown in the inset of Fig. 13(a). Across the visible spectrum, the first and second order diffracted output beams had positive and negative output coupling angles, θ, respectively; θ is defined in Fig. 13(a).

The TE and TM transmission spectra of the neurophotonic probe from the input fiber facet to the most distal grating coupler free space output are shown in Fig. 13(b). A photodetector was placed above the chip and aligned to either the first or second order diffracted beams. Above 540

Optics EXPRESS

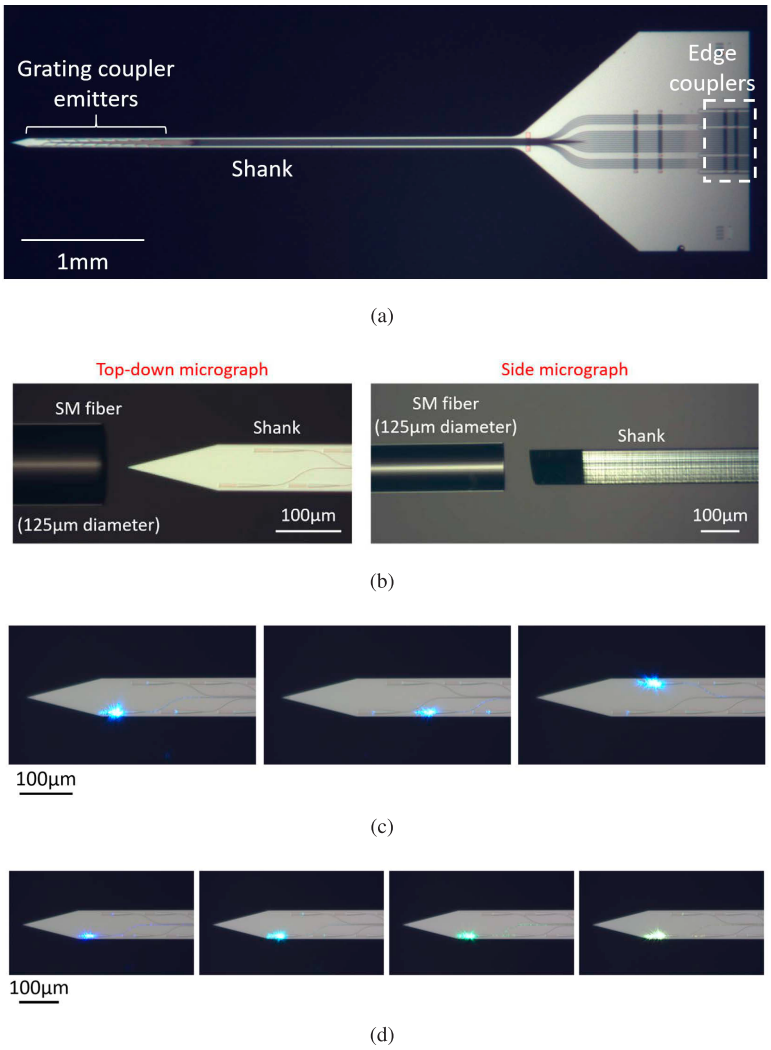

Fig. 12. (a) Optical micrograph of a neurophotonic probe chip. (b) Top-down and side optical micrographs of a probe shank next to a single-mode (SM) optical fiber (125 μm diameter). (c) Optical micrographs of a neurophotonic probe shank with different grating couplers emitting light at 488 nm. (d) Optical micrographs of the most distal grating coupler emitting light at 460 nm, 505 nm, 532 nm, and 580 nm.

Optics EXPRESS

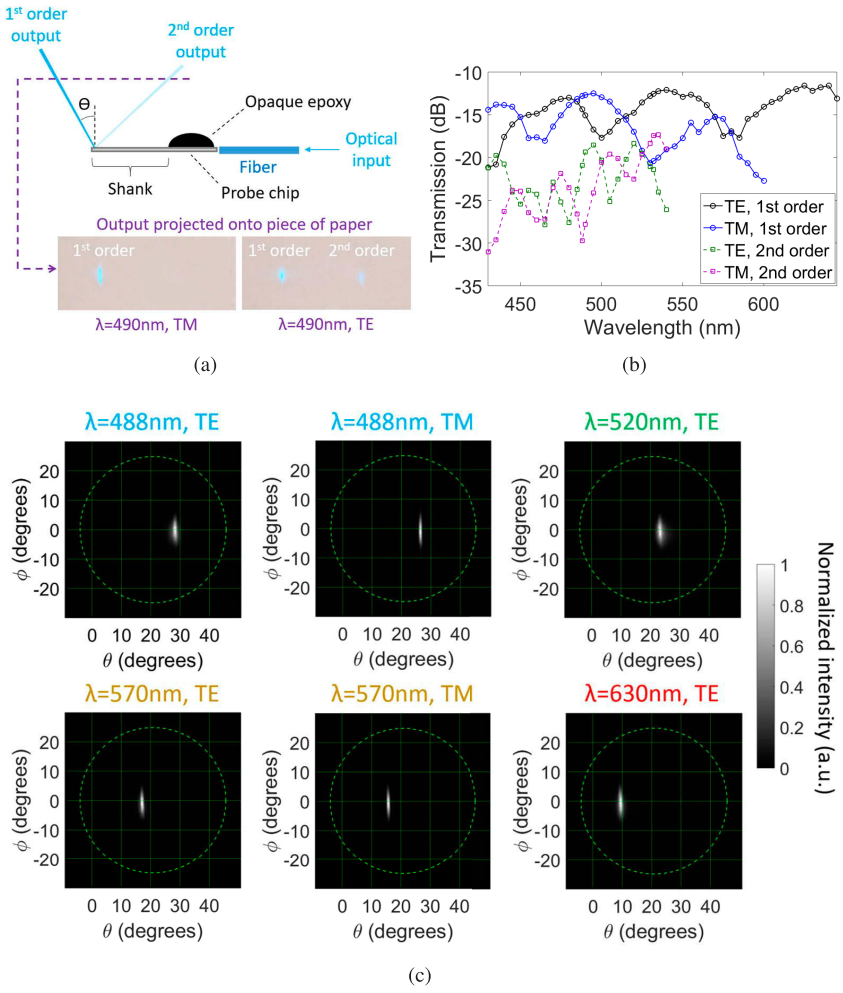

Fig. 13. Neurophotonic probe characterization. (a) Side-view schematic of the measurement configuration. Insets show photographs of the output light from one of the grating coupler emitters projected onto paper above the chip at 490 nm showing strong first order diffraction and weak second order diffraction for the TM polarization and stronger second order diffraction for the TE polarization. (b) Measured transmission of the most distal grating coupler emitter path on the probe chip (fiber facet to free space transmission for the first and second order diffraction output beams). (c) Measured far-field normalized intensity patterns of the most distal grating coupler emitter at wavelengths 488 nm, 520 nm, 570 nm, and 630 nm. The green dashed circle denotes the back aperture of the objective lens in the Fourier imaging system with a numerical aperture of 0.42.

Optics EXPRESS

nm, the coupling angle θ for the second order diffracted beam became too large and negative to be measured. The oscillations in the spectra are due to substrate reflections interfering with upwards radiation from the grating. The probe emitted light across the full measured wavelength range, 430-645 nm, with first order transmissions > -18 dB for the optimal polarization at each wavelength. Optimal wavelength spans exist for blue, green, and red operation, and by selecting the best polarization at each wavelength, first order transmission > -14 dB and suppression of the second order diffraction (relative to the first order) > 8 dB were observed over the wavelength ranges 470-495 nm and 530-540 nm; suppressions as high as 17 dB and 14 dB were measured over these wavelength ranges, respectively. First order TE transmission > -14 dB was measured from 605-645 nm, however, the second order diffraction was not measured at these wavelengths. Above 600 nm, the first order TM transmission became too low and difficult to distinguish from scattered light to be accurately measured, possibly due to a weak grating strength at these wavelengths for the TM polarization.

The far field radiation pattern of the most distal grating coupler was measured using the Fourier imaging system method in [22]. The Fourier imaging system had a measurement range of $\pm 24.8°$ and was angled along the θ axis at 21° to fit the first order diffracted beam into the Fourier imaging system angular range over the measured wavelength range. Measured far fields at various wavelengths and polarizations are shown in Fig. 13(c). ϕ is the angle out of the page in Fig. 13(a) perpendicular to θ. Low divergence beams were formed over the 430-645 nm wavelength range, and in the examples, the FWHM θ and ϕ divergences are $< 1.6°$ and $< 8°$, respectively. The θ divergence is determined by the grating period and duty cycle, and the ϕ divergence is determined by the grating socket width; these divergences can be engineered via the grating parameters to suit specific applications. Scattered light due to waveguide roughness can also contribute to the radiation profile of the probe, but the magnitude of the waveguide loss and large angular spread of this scattered radiation leads to an insignificant intensity compared to the grating coupler emission. This is evident from the absence of a significant background in Fig. 13(c). Outside the grating coupler emission pattern, the background intensity is < -23 dB (limited by camera noise) relative to the peak far field intensity of the grating. Fluorescein beam profiling of neurophotonic probes in [12,17] has also shown the contribution of waveguide scattering to be small.

Overall, the neurophotonic probe chip shows red, green, and blue light operation covering the excitation spectra of multiple opsins used in optogenetics (e.g., channelrhodopsin-2, halorhodopsin) [20,23] and common fluorophores used in fluorescence imaging and fluorescent calcium and voltage indicators used in functional imaging of brain tissue (e.g., green/yellow/red fluorescent proteins, GCaMP, RCaMP) [24–26]. The narrow beams generated by the probe are suited to illuminate small volumes of brain tissue for high resolution optogenetic stimulation and fluorescence imaging applications. The array of grating coupler emitters can be addressed via a multi-core fiber or image bundle and external scanning optics or spatial light modulators.

5. Conclusion

In conclusion, a visible light SiN waveguide platform was demonstrated on 200 mm Si wafers that have been thinned to ≈ 100 μm. Single and multimode waveguides, waveguide crossings, MMI power dividers, and neurophotonic probes were fabricated within the platform and characterized throughout the visible spectrum from 430-648 nm. Both PECVD and LPCVD SiN waveguides and devices were characterized, and low losses were observed in both cases. This platform and the devices demonstrated therein form a basis for more complex integration toward applications in bio/neurophotonics, display and imaging, and quantum information.

Optics EXPRESS

Appendix

The waveguide loss spectra of the 520-540 nm wide multimode waveguides in Figs. 4–6 have isolated spikes compared to the smoother loss spectra of narrow single mode waveguides. The origin of these spikes is the larger spectral ripples in the cutback structure transmission spectra, which is evident by comparing the transmission spectra in Figs. 14(a) and 14(b). The final extracted waveguide loss spectrum for the multimode waveguide is also more influenced by spectral ripple since the waveguide loss and the difference in transmission between cutback structures is lower. This spectral ripple is most likely due to excitation of multiple modes in the waveguides due to the bends and defects in the cutback structure waveguides. This hypothesis is supported by the observation that the narrow waveguides also have increased spectral ripple close to and below their single-mode cutoff wavelength, e.g., Fig. 14(a). However, the majority of the light in the multimode waveguide is expected to be in the fundamental mode since the output fiber coupling efficiency would be affected otherwise. Higher order mode excitation from input fiber coupling is prevented by a short length of single-mode waveguide following the edge coupler in the multimode cutback structures.

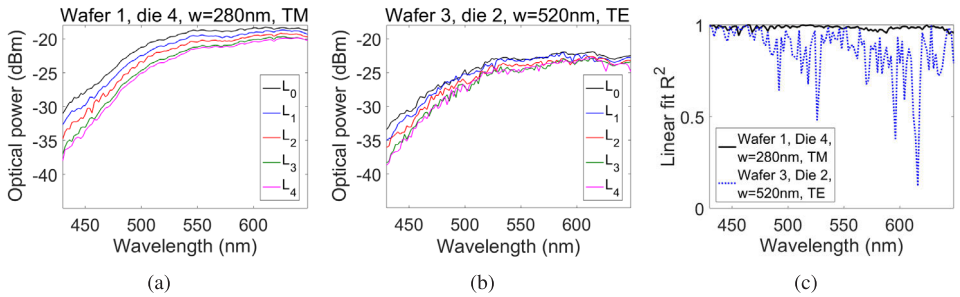

Fig. 14. (a), (b) Cutback structure output spectra from (a) 280 nm wide waveguides from die 4, Wafer 1 (TM polarization), (b) 520 nm wide waveguides from die 2, Wafer 3 (TE polarization). (c) R^2 of linear fits at each wavelength from (a) and (b).

The ripples of different cutback structures are not correlated, however, a small number of wavelength points may be affected by large notches or peaks in the transmission spectra of multiple cutback structures aligning and leading to a poor linear fit. The R^2 of linear fits are shown in Fig. 14(c). For the 520 nm wide multimode waveguide, $R^2 > 0.7$ and the standard error of the linear fit is < 1 dB/cm for 86% of the spectrum. For the 280 nm wide single-mode waveguide, $R^2 > 0.94$ for the entire spectrum. Overall, the spikes observed in the final waveguide loss spectra for the wide multimode waveguides and close to the single-mode cutoff wavelength of the narrow waveguides are an artifact of higher order modes in the cutback structures.

The method we used for measuring waveguide and device transmission spectra, Fig. 2(a), uses a tunable narrowband optical filter to filter the broad spectrum of a supercontinuum laser, effectively creating a tunable wavelength source across the visible spectrum. An optical detector measures the fiber-coupled output power as the wavelength is stepped, resulting in a transmission spectrum. We refer to this measurement procedure as Method 1. To verify the filter linewidth and extinction are sufficient for Method 1 to generate an accurate transmission spectrum, we also compared the results of Method 1 with Method 2, shown in Fig. 15(a). In Method 2, the fiber-coupled output from the chip is split into two fibers: one connected to a spectrometer with a resolution of < 0.3 nm, and the other connected to an optical detector. For each wavelength step of the filter, the maximum of the measured spectrometer spectrum is taken as the transmission, thus eliminating the influence of the filter linewidth and extinction. At each wavelength step,

Optics EXPRESS

the power at the optical detector is also recorded to generate a spectrum simultaneously using Method 1.

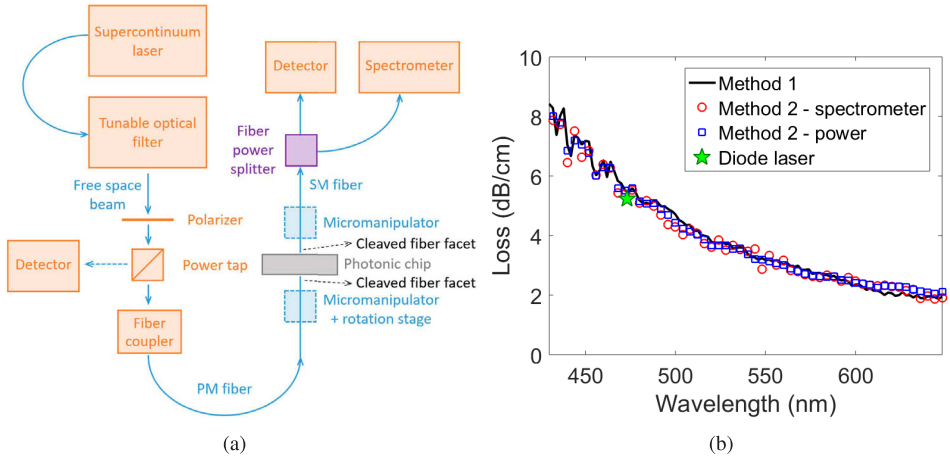

Fig. 15. (a) Schematic of Method 2 for measuring waveguide and device transmission spectra. (b) Comparison of waveguide loss spectra from Method 1, Method 2, and measurements with a 473 nm diode laser. Method 1 is shown in Fig. 2(a) and was used for all other measurements in this work. "'Method 2 - power"' refers to the waveguide loss spectra extracted from monitoring the optical detector in (a). The waveguides measured are 280 nm wide waveguides from die 5, Wafer 1, for TM polarized light.

Method 1 and Method 2 were compared for a small subset of the waveguide and device loss spectra measurements. Excellent agreement was observed in all cases. Figure 15(b) shows an example for 280 nm wide waveguides from die 5, Wafer 1, for TM polarized light. As a final comparison, light from a 473 nm diode laser was coupled to the chips via single-mode fiber (Nufern 460HP) and an inline fiber polarization controller, and the fiber-coupled output power was used for cutback measurements of a small subset of waveguides and devices. Excellent agreement was also observed with the diode laser measurement, which can also be seen in Fig. 15(b). Overall, the excellent agreement between all three measurement methods confirms the accuracy of our waveguide and device loss spectra measurements.

Funding

Canadian Institutes of Health Research (302353-381345); Natural Sciences and Engineering Research Council of Canada (CHRP 508406-17); National Institutes of Health (NS090596, NS099726); Kavli Nanoscience Institute.

Acknowledgments

We thank Dr. Huang Ying, Dr. Laurent Moreaux, Dr. Eran Segev, and Dr. Trevor Fowler for assistance and helpful discussions.

References

1. W. D. Sacher, J. C. Mikkelsen, Y. Huang, J. C. C. Mak, Z. Yong, X. Luo, Y. Li, P. Dumais, J. Jiang, D. Goodwill, E. Bernier, P. G.-Q. Lo, and J. K. S. Poon, "Monolithically integrated multilayer silicon nitride-on-silicon waveguide platforms for 3-D photonic circuits and devices," Proc. IEEE **106**(12), 2232–2245 (2018).
2. Q. Wilmart, H. El Dirani, N. Tyler, D. Fowler, S. Malhouitre, S. Garcia, M. Casale, S. Kerdiles, K. Hassan, C. Monat, X. Letartre, A. Kamel, M. Pu, K. Yvind, L. K. Oxenløwe, W. Rabaud, C. Sciancalepore, B. Szelag, and S. Olivier, "A versatile silicon-silicon nitride photonics platform for enhanced functionalities and applications," Appl. Sci. **9**(2), 255 (2019).

Optics EXPRESS

3. E. Timurdogan, Z. Su, C. V. Poulton, M. J. Byrd, S. Xin, R. Shiue, B. R. Moss, E. S. Hosseini, and M. R. Watts, "AIM process design kit (AIMPDKv2.0): Silicon photonics passive and active component libraries on a 300mm wafer," in *2018 Optical Fiber Communications Conference and Exposition (OFC)*, (2018), pp. 1–3.
4. https://towerjazz.com/technology/rf-and-hpa/silicon-photonics-rf/
5. A. Z. Subramanian, P. Neutens, A. Dhakal, R. Jansen, T. Claes, X. Rottenberg, F. Peyskens, S. Selvaraja, P. Helin, B. D. Bois, K. Leyssens, S. Severi, P. Deshpande, R. Baets, and P. V. Dorpe, "Low-loss singlemode PECVD silicon nitride photonic wire waveguides for 532-900 nm wavelength window fabricated within a CMOS pilot line," IEEE Photonics J. **5**(6), 2202809 (2013).
6. S. Romero-García, F. Merget, F. Zhong, H. Finkelstein, and J. Witzens, "Silicon nitride CMOS-compatible platform for integrated photonics applications at visible wavelengths," Opt. Express **21**(12), 14036–14046 (2013).
7. C. V. Poulton, M. J. Byrd, M. Raval, Z. Su, N. Li, E. Timurdogan, D. Coolbaugh, D. Vermeulen, and M. R. Watts, "Large-scale silicon nitride nanophotonic phased arrays at infrared and visible wavelengths," Opt. Lett. **42**(1), 21–24 (2017).
8. C. Sorace-Agaskar, S. Bramhavar, D. Kharas, W. Loh, P. W. Juodawlkis, J. Chiaverini, and J. M. Sage, "Multi-layer integrated photonics from the ultraviolet to the infrared," Proc. SPIE **10510**, 105100D (2018).
9. G. N. West, W. Loh, D. Kharas, C. Sorace-Agaskar, K. K. Mehta, J. Sage, J. Chiaverini, and R. J. Ram, "Low-loss integrated photonics for the blue and ultraviolet regime," APL Photonics **4**(2), 026101 (2019).
10. T.-J. Lu, M. Fanto, H. Choi, P. Thomas, J. Steidle, S. Mouradian, W. Kong, D. Zhu, H. Moon, K. Berggren, J. Kim, M. Soltani, S. Preble, and D. Englund, "Aluminum nitride integrated photonics platform for the ultraviolet to visible spectrum," Opt. Express **26**(9), 11147–11160 (2018).
11. S. Herwik, O. Paul, and P. Ruther, "Ultrathin silicon chips of arbitrary shape by etching before grinding," J. Microelectromech. Syst. **20**(4), 791–793 (2011).
12. W. D. Sacher, X. Liu, F.-D. Chen, H. Moradi-Chameh, I. F. Almog, T. Lordello, M. Chang, A. Naderian, T. M. Fowler, E. Segev, T. Xue, S. Mahallati, T. A. Valiante, L. C. Moreaux, J. K. S. Poon, and M. L. Roukes, "Beam-steering nanophotonic phased-array neural probes," in *Conference on Lasers and Electro-Optics* (Optical Society of America, 2019), p. ATh4I.4.
13. W. D. Sacher, X. Liu, I. F. Almog, A. Fomenko, T. Lordello, F.-D. Chen, H. Moradi-Chameh, A. Naderian, M. Chang, T. M. Fowler, T. A. Valiante, A. M. Lozano, L. C. Moreaux, J. K. S. Poon, and M. L. Roukes, "Nanophotonic neural probes for in vivo light sheet imaging," in *Conference on Lasers and Electro-Optics* (Optical Society of America, 2019), p. SM4H.6.
14. H. Chen and A. W. Poon, "Low-loss multimode-interference-based crossings for silicon wire waveguides," IEEE Photonics Technol. Lett. **18**(21), 2260–2262 (2006).
15. L. B. Soldano and E. C. M. Pennings, "Optical multi-mode interference devices based on self-imaging: principles and applications," J. Lightwave Technol. **13**(4), 615–627 (1995).
16. E. Shim, Y. Chen, S. Masmanidis, and M. Li, "Multisite silicon neural probes with integrated silicon nitride waveguides and gratings for optogenetic applications," Sci. Rep. **6**(1), 22693 (2016).
17. E. Segev, J. Reimer, L. C. Moreaux, T. M. Fowler, D. Chi, W. D. Sacher, M. Lo, K. Deisseroth, A. S. Tolias, A. Faraon, and M. L. Roukes, "Patterned photostimulation via visible-wavelength photonic probes for deep brain optogenetics," Neurophotonics **4**(1), 011002 (2016).
18. S. Libbrecht, L. Hoffman, M. Welkenhuysen, C. Van den Haute, V. Baekelandt, D. Braeken, and S. Haesler, "Proximal and distal modulation of neural activity by spatially confined optogenetic activation with an integrated high-density optoelectrode," J. Neurophysiol. **120**(1), 149–161 (2018).
19. A. Mohanty, Q. Li, M. A. Tadayon, G. R. Bhatt, E. Shim, X. Ji, J. Cardenas, S. A. Miller, A. Kepecs, and M. Lipson, "An active visible nanophotonics platform for sub-millisecond deep brain neural stimulation," in *Conference on Lasers and Electro-Optics* (Optical Society of America, 2018), p. ATh3Q.1.
20. K. Deisseroth, "Optogenetics: 10 years of microbial opsins in neuroscience," Nat. Neurosci. **18**(9), 1213–1225 (2015).
21. A. N. Zorzos, J. Scholvin, E. S. Boyden, and C. G. Fonstad, "Three-dimensional multiwaveguide probe array for light delivery to distributed brain circuits," Opt. Lett. **37**(23), 4841–4843 (2012).
22. J. Sun, E. Timurdogan, A. Yaacobi, E. S. Hosseini, and M. R. Watts, "Large-scale nanophotonic phased array," Nature **493**(7431), 195–199 (2013).
23. X. Han, "In vivo application of optogenetics for neural circuit analysis," ACS Chem. Neurosci. **3**(8), 577–584 (2012).
24. R. N. Day and M. W. Davidson, "The fluorescent protein palette: tools for cellular imaging," Chem. Soc. Rev. **38**(10), 2887–2921 (2009).
25. T.-W. Chen, T. J. Wardill, Y. Sun, S. R. Pulver, S. L. Renninger, A. Baohan, E. R. Schreiter, R. A. Kerr, M. B. Orger, V. Jayaraman, L. L. Looger, K. Svoboda, and D. S. Kim, "Ultrasensitive fluorescent proteins for imaging neuronal activity," Nature **499**(7458), 295–300 (2013).
26. H. Dana, B. Mohar, Y. Sun, S. Narayan, A. Gordus, J. P. Hasseman, G. Tsegaye, G. T. Holt, A. Hu, D. Walpita, R. Patel, J. J. Macklin, C. I. Bargmann, M. B. Ahrens, E. R. Schreiter, V. Jayaraman, L. L. Looger, K. Svoboda, and D. S. Kim, "Sensitive red protein calcium indicators for imaging neural activity," eLife **5**, e12727 (2016).